RESEARCH ARTICLE

VOLCANICA

Experimental investigation of volcaniclastic compaction during burial

Edgar U. Zorn*, Jackie E. Kendrick, Anthony Lamur, Janine Birnbaum, Ulrich Kueppers, Marize Muniz da Silva, and Yan Lavallée

Earth and Environmental Sciences, Ludwig-Maximilians-Universität München, Theresienstraße 41, 80333 München, Germany.

Submitted: 2024-06-27 | Accepted: 2024-10-04 | Published: 2024-11-22

Editor: A Kushnir | Typesetter: J Farquharson

Abstract

Volcanic deposits compact and deform following emplacement and burial. Here, we experimentally investigate the compaction of volcaniclastic material through gravitational loading (i.e. burial). Two lithologies (scoria and hyaloclastite) of different grain size (ash and lapilli) were held in a cylindrical container and compressed between two pistons to target stresses of 2, 5, 10, or 20 MPa, whilst monitoring axial displacement and acoustic emissions, enabling quantification of strain, densification, and comminution. In a second suite of experiments, samples were loaded and held at each stress to creep for six hours. The density and porosity of all samples were measured pre- and post-experiment. For all experiments, most deformation occurred during the early loading phase, then strain rates diminished with increasing compaction. During early loading, the hyaloclastite compacted faster than the scoria, but due to efficient early compaction, deformed more slowly at higher stresses and during creep. Grain size was also important for the amount of compaction; lapilli samples were initially less efficiently packed than ash samples and accumulated higher strain during the early part of loading. The strain experienced by all samples was substantial: even 2 MPa (equivalent to an overburden of ~180–230 m for our porous lithologies) caused volume reductions of 10–30 % due to grain rearrangement and crushing. Interpolation and extrapolation of the data were used to forecast instantaneous and time-dependent surface deformation of volcaniclastic deposits of different thicknesses. The findings yield important new constraints for the interpretation of ground deformation signals and development of models of volcanic flank instability.

Keywords: Load compaction; Volcaniclastic deposit; Volcano subsidence; Creep deformation; Grain comminution.

1 Introduction

Volcanic deposits are known to deform for years to decades after their emplacement [e.g. Wittmann et al. 2017]. At active volcanoes, long-term flank motion constitutes a significant hazard, as the associated deformation may be a cause or consequence of structural instability [e.g. Chen et al. 2017; Zorn et al. 2023]. However, the interpretation of deformation signals is still challenging due to the variable contribution of magmatic/hydrothermal unrest, compaction of erupted volcanic deposits, and flank motion [e.g. Schaefer et al. 2019]. At volcanoes, ground subsidence is commonly attributed to (1) cooling contraction [Wittmann et al. 2017], (2) degassing and crystallisation [Caricchi et al. 2014], (3) flow of magma or hydrothermal fluids and associated alteration [Caricchi et al. 2014; Gottsmann et al. 2022], (4) cataclastic flow of porous volcanic rocks [Heap et al. 2015; Eggertsson et al. 2020], or (5) thermal degradation of materials adjacent to magmas [Castagna et al. 2018; Weaver et al. 2020]. However, the compaction of volcaniclastic deposits through gravitational loading (i.e. the stress imparted during burial by subsequent eruptive deposits) is often overlooked as a potential source of ground deformation, in part, because a quantitative description of such a process, both in the field and in laboratory experiments, remains incomplete.

Studies on gravitational load compaction of non-volcanic granular (clastic) materials and soils are abundant in the geoengineering literature [see Nawaz et al. 2013; Kodikara et al. 2018 for reviews], but for soils, many of the standardised tests commonly employed only consider low burial stresses (e.g. oedometers are used to test in the kPa range), as these are the prevalent values relevant for agriculture or the construction of infrastructure (i.e. for buildings, roads, etc.). For granular geomaterials the focus is often on loose or disaggregated sand at intermediate confining pressures for the consideration of geoengineering challenges or accessing resources [e.g. Parkin 1991; Hagin and Zoback 2004; Karner et al. 2005; Ma et al. 2014], and these tend to consist of monomineralic grains. In contrast, volcaniclastic deposits often comprise heterogeneous and porous grains and can be buried by up to a few kilometers by the accumulation of erupted materials. Burial rates can vary greatly as volcanic deposits accumulate either slowly and gradually (e.g. ash accumulation over months to centuries) or suddenly in large volume eruptions (depositing hundreds of meters of material within minutes to hours), and overburden may reach up to tens of MPa). Another key difference between volcaniclastic rocks and other clastic systems is in the nature of the clasts themselves. Volcanic materials typically contain varying fractions of vesicles (0–97 %), which greatly affects their strength [see Heap and Violay 2021; Lavallée and Kendrick 2021 for reviews]. Therefore, volcaniclastic deposits with high intra-granular porosity are more prone to compaction through grain crushing compared to monomineralic grains or soils.

The mechanical properties of volcaniclastic materials have been experimentally studied, but most commonly on pyroclastic systems at high temperature undergoing sintering and/or compression [e.g. Quane et al. 2009; Vasseur et al. 2013; Kendrick et al. 2016] or clast abrasion and comminution during transport [e.g. Kueppers et al. 2012; Mueller et al. 2015; Hornby et al. 2020]. Fewer studies deal with volcaniclastic deposits at ambient conditions, focusing on shear- and frictional properties [Moore et al. 2008; Boldini et al. 2009; Rotonda et al. 2010; Lavallée et al. 2014; Sassa et al. 2014], whereas deposit com-

* e.zorn@lmu.de

paction in response to gravitational loading—the topic of this study—has rarely been investigated [Rotonda et al. 2010; Bai et al. 2023]. Bai et al. [2023] studied the compaction of basaltic scoria samples from Hongtu Hill (Changbaishan Area, China) and identified that compaction is primarily accommodated by grain packing at low stresses (10–30 MPa) and comminution (i.e. particle crushing) at high stresses (50–70 MPa). As vesicularity can vary widely between pyroclasts, we hypothesise that these regimes should overlap depending on the characteristics of the clasts. In this study, we experimentally investigate the mechanical, physical, and acoustic characteristics of volcaniclastic material compaction under dynamic and static stress conditions representative of shallow volcanic environments. The observed dynamics of compressing volcanic materials provide insights into the development of ground subsidence and flank instability at volcanoes.

2 Methods and materials

2.1 Materials

We selected two volcanic rock types to produce granular samples with similar grain morphology. The first material (herein referred to as scoria) consists of fragments crushed from porous basanitic lava flows quarried in the East Eifel volcanic field, Germany, selected to be representative of materials found on young scoria cones. It has been used in previous experimental studies [Douillet et al. 2014; Cigala et al. 2017]. The grains typically host phenocrysts of pyroxene and olivine in a micro-crystalline groundmass (Figure 1A) and contain round, sometimes interconnected vesicles, µm to mm in size. Overall, the textural variability of the grains is high (Figure 1A and Supplementary Material 1 Figures S1A, S1B, S2A, S2B). The second material consists of crushed hyaloclastite, collected from the explosive products of the Víti crater at Krafla caldera, Iceland. The material has been used in previous thermo-mechanical studies [Eggertsson et al. 2020; Weaver et al. 2020]. The hyaloclastite consists of indurated fragments of basalt (of ash to lapilli size) containing abundant phenocrysts and a groundmass consisting dominantly of interstitial glass and minor microlite content (Figure 1B). Alteration minerals are observed to coat the surface area and fill the pore space of some clasts and are known to consist of chabazite, smectite and quartz [Weaver et al. 2020]. The hyaloclastite contains typically small (<300 µm) and irregularly shaped vesicles, as well as complex networks of fractures and intragranular pore space, which promotes a range of textures and porosities in the crushed, tested grains (Figure 1B). Pore spaces are frequently filled up by alteration minerals (Supplementary Material 1 Figure S2C, S2D) which appear as a yellow-brown coating on the surface (Supplementary Material 1 Figure S1C, S1D).

2.2 Sample preparation

The crushed scoria and hyaloclastite samples were first oven dried at 60 °C overnight (>12 hours), to eliminate residual moisture. To test the impact of grain sizes on compaction, both sample lithologies were then dry sieved into two grain size populations: the finer-grained sample consists of medium-to-coarse ash (0.5–2 mm), the coarse-grained sample of fine-to-medium lapilli (2–4 mm). For this, we used three sieves (0.5, 2, and 4 mm) in a Retsch AS 200 sieve shaker, which produced vibrations for 20 minutes at a vibrational amplitude per gravitational acceleration of 1.5 mm$\cdot\vec{g}^{-1}$; every 20 s vibrations automatically stopped for ~1.5 s to allow grains to fall through the meshes. The finer portions (below 0.5 mm) were discarded. This removed most of the clay minerals in the hyaloclastites, which tended to form very fine particles during crushing and sieving.

For measuring solid densities and isolated porosities, a subset of granular aggregate material from both lithologies was crushed into a fine powder using a ring and puck mill. To investigate the physical properties of single grains (in particular grain porosity, which is likely to influence grain crushing during compaction), we also drilled and cut cylindrical cores from individual grains of both lithologies. For this we primarily used grains larger than the sieved portions and obtained 10 cores (2.8–5.0 mm diameter, 2.0–5.6 mm height range) per lithology to account for variability between different grains.

2.3 Sample characterisation

After sieving, key physical properties were characterised, including:

- Bulk density, ρ_b, refers to the density of the granular aggregate loaded in our experimental assembly. We first measured the mass, m, of the aggregate using a set of scales with an accuracy of ± 0.01g. We then placed it in a cylindrical cup (51.2 mm diameter, 99.2 mm height) before gently tapping the cup to ensure a flat surface at the top. We finally measured the depth of the flat surface with a calliper to obtain the cylindrical height of the pack to calculate the bulk volume of the experimental charge, V_b. Due to the irregular surface of granular samples, we tested the variability of the depth measurements by repeating them 10 times for one sample of each population and determined a standard deviation on the length measurements of ~1.5 % for lapilli and 0.5 % for ash samples. The bulk density was calculated with:

$$\rho_b = \frac{m}{V_b}. \tag{1}$$

- Solid density, ρ_s, refers to the density of the rock mass using milled (pore free) powder. We measured the volume, V_s, of the powder using a Quantachrome Ultrapyc 1200e helium pycnometer, which offers an accuracy of ± 0.02 vol.%. The solid density was calculated via:

$$\rho_s = \frac{m}{V_s}. \tag{2}$$

- We also calculated the skeletal density, ρ_{sk}, of the granular aggregates (unpowdered). The skeletal volume V_{sk}, which includes the solid fraction and isolated pores within the grains, is measured for a mass m using the helium pycnometer:

$$\rho_{sk} = \frac{m}{V_{sk}}. \tag{3}$$

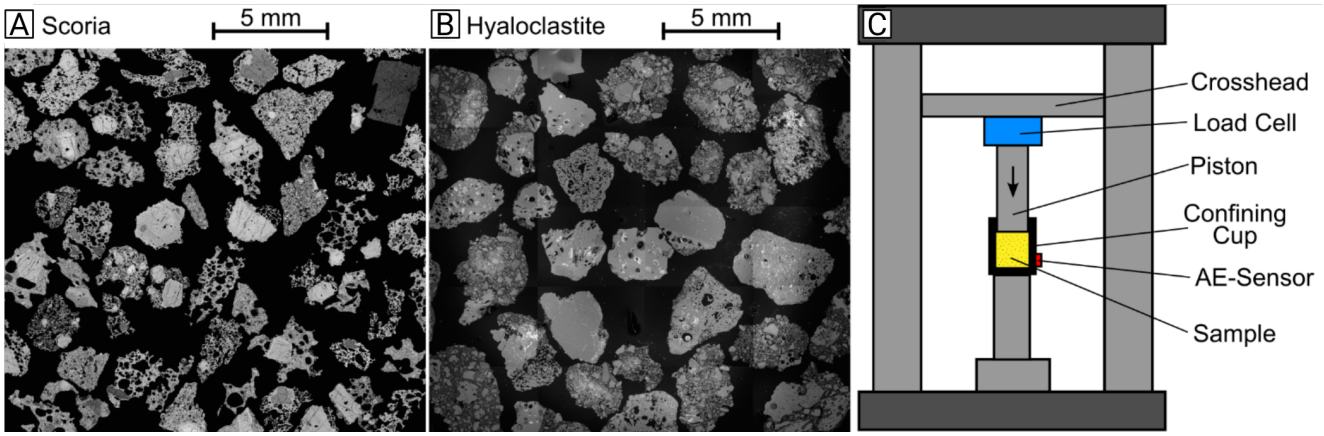

Figure 1: Experimental components. [A–B] Backscattered electron (BSE) images of [A] the scoria and [B] the hyaloclastite in the lapilli grain size, taken using a scanning electron microscope (Hitachi SU5000) on epoxy-suspended grains (epoxy is black) with a cut and polished surface. [C] Sketch of the experimental setup, showing the sample assembly held in a uniaxial press.

• As the materials also contain isolated pores, ϕ_I, (which contributes to the skeletal density value as they are by definition inaccessible) we quantified the isolated porosity, via:

$$\phi_I = \frac{\rho_s - \rho_{sk}}{\rho_s} \times 100. \quad (4)$$

• Bulk porosity, ϕ_b, refers to the percentage of connected voids of the bulk granular aggregate loaded in our experimental assembly (i.e. intergranular and intragranular pore space, but excluding isolated pores). This was determined by the ratio of skeletal and bulk sample densities using:

$$\phi_b = \frac{\rho_b - \rho_{sk}}{\rho_b} \times 100. \quad (5)$$

• Grain porosity, ϕ_s, refers to the percentage of connected voids (including vesicles and fractures) within individual grains, which can be determined for uniform shapes with defined volume. We measured the mass (an accuracy of ±0.001 g) and calculated the cylindrical volume, V_{bc} of each of the 10 grain cores (using callipers). The skeletal volume of the cores V_{sk} was measured using a Micromeritics AccuPyc II 1340 helium pycnometer, equipped with a chamber of 1.3351 cm^3, which provides an accuracy of ±0.01 vol.%. We calculated the grain porosity via:

$$\phi_s = \frac{V_{bc} - V_{sk}}{V_{bc}} \times 100. \quad (6)$$

• Void ratio is commonly used to analyse granular materials [e.g. Monkul and Ozden 2007; Mesri and Vardhanabhuti 2009; Kodikara et al. 2018]. Void ratio e refers to the ratio of void volume (V_v) to the skeletal volume of the bulk sample (V_{sk}), measured for the granular aggregate within our sample assembly. V_v was calculated by subtracting the measured skeletal volume (V_{sk}) from the measured bulk volume (V_b) of the experimental charge ($V_v = V_b - V_{sk}$), so that:

$$e = \frac{V_v}{V_{sk}}. \quad (7)$$

• Grain size distribution: We quantified the grain size distribution of our sample populations (ash and lapilli) before and after compaction experiments. For this, we used the same sieve tower and settings as for sample preparation, but with additional sieve sizes (4.0, 2.8, 2.0, 1.4, 1.0, 0.71, 0.50, 0.25, 0.125, 0.063 mm). After shaking the sample assembly for 20 min (see above for further details), the fractions collected from each sieve were weighed to assess the grain size distribution.

• Polydispersivity: Using our grain size distribution results, we further calculate the degree of polydispersivity following Torquato and Haslach [2002]:

$$S = \frac{\langle R \rangle \times \langle R^2 \rangle}{\langle R^3 \rangle}, \quad (8)$$

where S is the polydispersivity index (1 representing monodisperse, 0 representing fully polydisperse) and where $\langle R \rangle$, $\langle R^2 \rangle$, and $\langle R^3 \rangle$ are the mean, variance, and skewness of the distribution (or 1st, 2nd, and 3rd moments of the radial distribution, respectively).

2.4 Compaction experiments

We used an Instron 5969 uniaxial press with a 50 kN load cell to compact our volcaniclastic samples (Figure 1C). The sample assembly consists of a cylindrical metal cup (42 mm inner diameter, 59.4 mm height) filled to a height of ~43 mm with granular materials of one rock type (i.e. hyaloclastite or scoria) and a given grain size (i.e. ash or lapilli). The cup was placed onto the lower piston of the press and the upper piston (40 mm diameter) was then lowered into the cup and onto the sample to load it; the press controlled the load and monitored the piston position (i.e. axial displacement). Load was thereby converted to stress, considering the piston diameter. Prior to experiments, compliance tests were carried out to measure the deformation of the load chain (piston assembly and the empty cup). The deformation associated

with system compliance was subtracted from our experimental datasets to accurately quantify the sample deformation as a function of applied stress. The corrected displacement was used to calculate axial strain (shortening) experienced by the sample throughout all experiments. Due to the different diameters between piston and sample cup, there was a 1 mm gap around the piston, preventing frictional contact between the two. After experiments it was visually verified that no sample material had entered the gap.

The stressing of fragmental materials in a rigid metal cup (presuming negligible radial deformation) effectively simulates the compaction of volcaniclastic deposits that are laterally restricted and deformed by overburden. As the cup cannot deform, the piston displacement served to reduce bulk sample volume, thereby providing a real-time quantification of volumetric strain. This geometrical simplification also enabled the quantification of changes in bulk density, bulk porosity, and void ratio from the measured axial and so, volumetric strains (via Equation 1, 5, and 7).

Two sets of compaction experiments were conducted on all four sample populations: (i) dynamic stressing tests (or loading) and (ii) static stress tests (termed creep). For the dynamic stressing tests, we applied a constant stress rate of 0.1 MPa·min^{-1} until a target stress (2, 5, 10, 20 MPa) was reached, after which samples were unloaded and collected for analysis. For the static stress tests, the samples were equally loaded at 0.1 MPa·min^{-1} and once at target stress (2, 5, 10, 20 MPa), the applied stress was held constant for 6 hours to constrain progressive compaction during creep deformation. To gauge creep compaction for longer timescales, one additional experiment (using lapilli scoria) was performed at 2 MPa static stress for ~5 days.

The monitored mechanical data (stress and strain) were used to calculate key indices of granular sample compaction: the compression index (C_c; Equation 9) for the dynamic stressing (at constant stress rate) and the secondary compression index (C_α; Equation 10) under static stress conditions (creep) following Augustesen et al. [2004], Monkul and Ozden [2007], and Mesri and Vardhanabhuti [2009]:

$$C_c = -\frac{\Delta e}{\Delta \log(\sigma)} \quad (9)$$

$$C_\alpha = -\frac{\Delta e}{\Delta \log(t)} \quad (10)$$

which accounts for changes in void ratio Δe, as a function of the dynamic stress σ or creep duration t and is calculated using tangents on (near) linear intervals of e vs $\log(\sigma)$ or $\log(t)$, respectively. These indices express the irreversible non-elastic compression, generally encountered beyond the pre-compression stress, σ_P, (otherwise termed pre-consolidation stress) which is marked by an inflection in the e vs $\log(\sigma)$ plot [Keller et al. 2011]. We here determined σ_P for the dynamic experiments by tracing the intersection of two tangents before and after the inflection, with the slope of the tangent after the inflection being that which determines C_c. In the static tests, C_α is picked for the last three hours of data at constant stress.

During the experiments, we monitored acoustic emissions (AEs) using a high sensitivity R50S piezoelectric transducer attached to the lower side of the confining cup holding the sample. The AE sensor was connected via a 2/4/6 preamplifier (set to a 40 dB threshold with a 20 dB gain) to a PCI-2 data acquisition system developed by Physical Acoustics Corporation. This enabled detection of acoustic signals released when grains ruptured and/or slid (i.e. upon grain reorganisation), providing insights into the timing of such signals during compaction.

3 Results

3.1 Material properties

The results of the sample characterisation are summarised in Table 1. The scoria is characterised by a higher solid powder density ρ_s (3.11 g·cm^{-3}) than the hyaloclastite (2.75 g·cm^{-3}). Skeletal solid densities ρ_{sk} are essentially equivalent for the scoria (3.10 g·cm^{-3}), but slightly lower for the hyaloclastite (2.67 g·cm^{-3}), indicating that the latter contains a minor fraction of isolated pores ϕ_I (2.6 %). The scoria has a slightly higher average grain porosity ϕ_s (36.0±15.9 vol.%) compared to the hyaloclastite (30.6±9.4 vol.%); in both cases, the observed variabilities reflect the inhomogeneity across the assemblages, as supported by BSE images (Figure 1A, 1B). Once sieved to their respective grain sizes, the lithologies have comparable, low bulk densities ρ_b with the lapilli populations consistently having a lower density (0.89–0.97 g·cm^{-3}) than the ash populations (1.04–1.14 g·cm^{-3}) in the scoria and hyaloclastite. Correspondingly, the bulk porosities ϕ_b were higher for both lapilli samples (67–69 %) than the ash (61–63 %).

3.2 Compaction during dynamic stressing tests

The loading curve of granular materials was characterised by a volume reduction for all samples as strain initially rapidly increased with stress before slowing progressively (Figure 2A). The corresponding strain rate decreased non-linearly throughout stressing (Figure 2B). This resulted in bulk porosity decreasing non-linearly (Figure 2C), and correspondingly, to non-linear increases in bulk density (Figure 2D) for all samples. Each sample suite showed a distinct response to stressing. Multiple experiments for each material show very little variation for a given parameter (e.g. strain, strain rate, bulk density, bulk porosity, void ratio) through dynamic stressing (Supplementary Material 1 Figures S3, S4 and Supplementary Material 1 Table S1), which indicate the reliability of the testing methods to characterise the compaction of different lithologies.

Grain size impacted the compactional behaviour of the granular aggregates; for both lithologies, the lapilli population accumulated more strain than the ash (Figure 2A). Compaction rates were higher in lapilli during the initial stages of loading but the rates slowed more significantly than the ash samples for both lithologies (Figure 2B). Hyaloclastites of both grain sizes initially accumulated more compactional strain than the scoria during early loading (Figure 2A). During the early part of loading (<2 MPa) strain rates were higher for the hyaloclastite but at higher stress, the rates slowed more due to efficient early compaction and the rates of compaction of the scoria were higher from ~2–3 MPa onwards (Figure 2B).

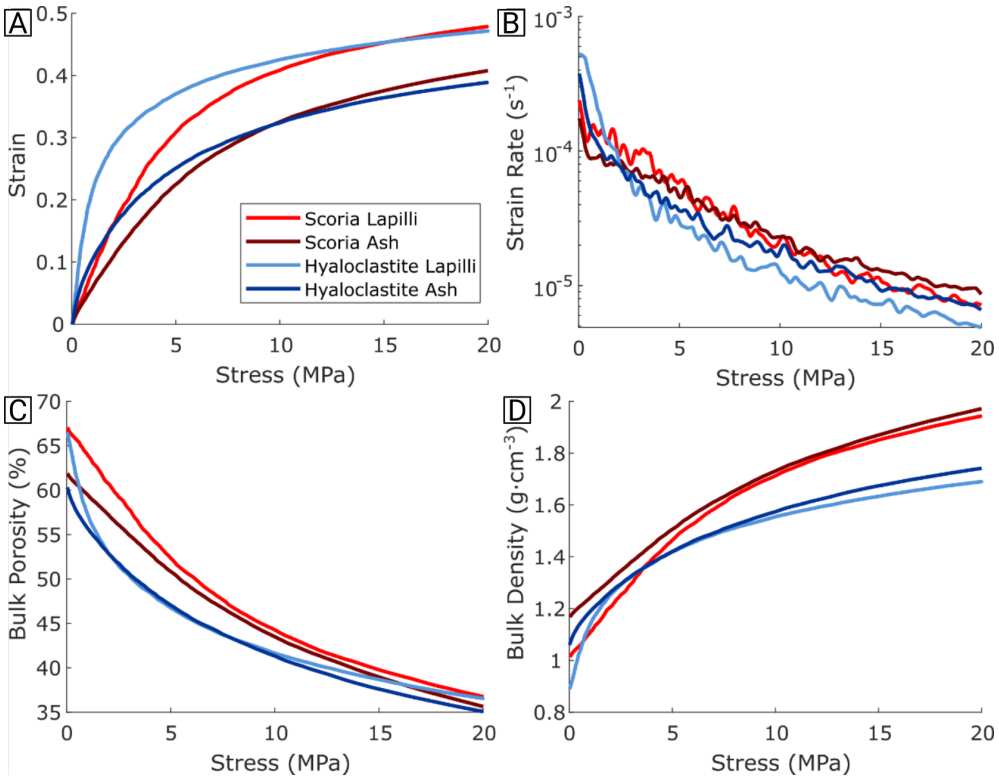

Figure 2: Compaction of volcaniclastic samples during dynamic stressing tests. Evolution of [A] strain [B] strain rates, [C] bulk porosities and [D] bulk densities with stress. To reduce noise in the calculated strain rates, we smoothed the datasets using 30 s sampling intervals and a 5 min moving window average. The figure only shows the data obtained from dynamic stressing experiments reaching 20 MPa; the data for experiments reaching lower stresses (2, 5, 10 MPa) can be found in Supplementary Material 1 Figures S3, S4.

Table 1: Sample properties measured before compaction. The solid density was obtained on a single powdered sample, all other values are presented as averages, from repeat measurements on both bulk aggregate and single grains, accompanied by standard deviations.

Material property	Scoria		Hyaloclastite	
Aggregate powder density ρ_s (g·cm^{-3})	3.11		2.75	
Aggregate skeletal density ρ_{sk} (g·cm^{-3})	3.10 ± 0.01		2.67 ± 0.01	
(Connected) Grain density ρ_{sc} (g·cm^{-3})	3.03 ± 0.14		3.02 ± 0.07	
(Connected) Grain porosity ϕ_s (%)	36.0 ± 15.9		30.6 ± 9.4	
Aggregate isolated porosity ϕ_I (%)	0.9 ± 0.4		2.6 ± 0.4	
Initial grain size (mm)	Lapilli: 2–4	Ash: 0.5–2	Lapilli: 2–4	Ash: 0.5–2
Aggregate bulk density ρ_b (g·cm^{-3})	0.97 ± 0.05	1.14 ± 0.04	0.87 ± 0.03	1.04 ± 0.02
Aggregate bulk porosity ϕ_b (connected, %)	68.7 ± 1.6	62.9 ± 1.2	67.2 ± 0.9	61.2 ± 0.7
Aggregate void ratio e	2.10 ± 0.16	1.70 ± 0.09	2.05 ± 0.08	1.58 ± 0.05

Grain size also appears to exert an influence on the evolution of bulk porosity and density under applied stress; upon initial stressing, the bulk porosity of lapilli samples reduced more readily than the ash (Figure 2C), whilst the bulk density correspondingly increased more rapidly upon stressing lapilli samples than ash samples (Figure 2D). More notably, the bulk porosity reduction and bulk density increase is largely dependent on the lithology, with the hyaloclastite initially decreasing faster in porosity and increasing faster in density compared to the scoria (Figure 2C, 2D). At the end of all tests, bulk porosities of all samples reduced to the same narrow range (35–37 %), whereas bulk densities increased differentially by lithology (~1.9 g·cm^{-3} for scoria; ~1.7 g·cm^{-3} for hyaloclastites) due to their contrasting solid densities (Table 1).

3.3 Compaction during static stress tests

In this second set of experiments, the samples were loaded at the same rate used in the dynamic test until a target stress (up to 2, 5, 10, or 20 MPa) at which they were held for 6 hours. During loading, the samples had equivalent behaviour to the dynamic stress tests (Figure 2; Supplementary Material 1 Fig-

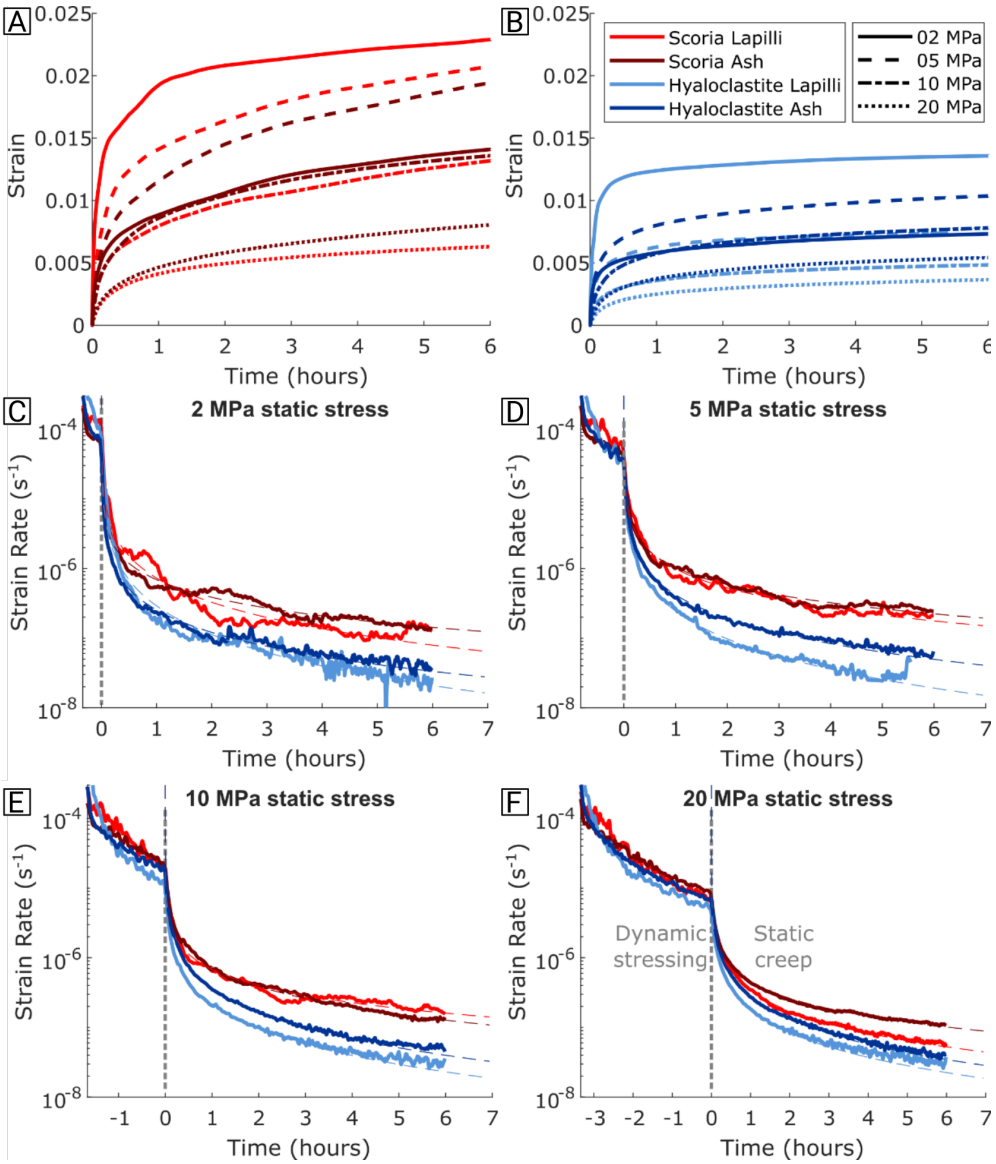

Figure 3: Compaction of volcaniclastic samples during static stressing tests. Strain evolution of [A] scoria and [B] hyaloclastite during creep only (set as zero at the onset of static stress) at the different applied static stresses (indicated by different line formats in the key in panel b). Strain rate evolution during the initial dynamic stressing and the subsequent static stress for tests undertaken at [A] 2 MPa, [B], 5 MPa, [C] 10 MPa, and [D] 20 MPa for the four sample populations (colour-coded as per the key in panel [B]). Note that time 0 is designated at the start of the static stress. Dashed lines in panels [C]–[F] mark fitted curves used in creep models presented in the Application to Field Scale Section.

ures S3, S4). At the target constant stress, the samples compacted through time (i.e. creeped). Most of the creep strain was accumulated in the first ~20 minutes at all conditions (Figure 3A, 3B). This deformation promoted higher initial strain rates which non-linearly decreased for all samples (Figure 3C–3F). The applied static stress strongly controlled the evolution of creep strain. With an increase in applied static stress, the samples typically accumulated lower creep strain through time (Figure 3A, 3B) which can be attributed to the high magnitude of strain already experienced during loading (Figure 3C–3F). However, both ash samples appear to slightly differ from this general trend as the lowest static stress of 2 MPa resulted in lower creep strains than 5 MPa (Figure 3A, 3B). Comparing lithologies, the scoria underwent more creep than the hyaloclastite under a given stress (Figure 3A, 3B), and correspondingly the strain rates for the hyaloclastites were thus slower than the scoria at all conditions (Figure 3C–3F). During the early stages of creep strain rates reduced more rapidly in the hyaloclastites (than scoria) from comparable rates at the end of dynamic stressing (Figure 3C–3F). The effect of grain size on creep was complex; lapilli populations accumulated significantly higher creep strain than ash at low stress (2 MPa for hyaloclastite, and 2–5 MPa for the scoria). At higher stresses, the reverse was found and ash compacted more than lapilli (Figure 3A, 3B). The strain rates provided further information as to the disparate compactional behaviour

Table 2: Monitored data during the creep stress, including the average rate of acoustic emissions (AEs in counts·min^{-1}), and averaged strain rates ($\dot{\varepsilon}$ in s^{-1}) for the final 30 minutes of creep, and the secondary compression index (C_α) measured during the final 3 hours of creep. The AEs of the hyaloclastite ash at 10 MPa were not measured.

		Scoria		Hyaloclastite	
		Lapilli	Ash	Lapilli	Ash
AEs (counts·min^{-1})	2 MPa	4	141	20	63
	5 MPa	259	211	91	75
	10 MPa	278	278	95	-
	20 MPa	137	164	223	417
$\dot{\varepsilon}$ (s^{-1})	2 MPa	1.43×10^{-7}	1.75×10^{-7}	2.51×10^{-8}	4.03×10^{-8}
	5 MPa	2.28×10^{-7}	2.87×10^{-7}	3.19×10^{-8}	6.12×10^{-8}
	10 MPa	2.31×10^{-7}	1.32×10^{-7}	3.15×10^{-8}	5.19×10^{-8}
	20 MPa	6.07×10^{-8}	1.12×10^{-7}	3.16×10^{-8}	4.01×10^{-8}
C_α	2 MPa	0.0161	0.0187	0.0046	0.0053
	5 MPa	0.0320	0.0323	0.0048	0.0091
	10 MPa	0.0342	0.0234	0.0063	0.0083
	20 MPa	0.0156	0.0235	0.0079	0.0092

of ash and lapilli; the lapilli tended to compact at faster rate in the early part of static stressing at low stresses (Figure 3C, 3D), but as time progressed ash typically creeped faster than lapilli for both lithologies at all conditions (Figure 3C–3F). This is attributed to the evolution in strain rate during dynamic stressing (Figure 2B), where lapilli compact more efficiently under initial loading and thus, have already compacted more substantially prior to reaching the target stress of the static tests, particularly at >10 MPa (Figure 3C–3F). Although strain rates decreased through time, we observed that no sample had stopped compressing at the end of the six hours of static stress tested herein. The additional five-day static stress experiment indicated that the rate of compaction continued to reduce (Supplementary Material 1 Figure S5).

3.4 Acoustic signals during dynamic and static stressing

The compaction of volcaniclastics released acoustic emissions. We observed that the majority (~72–93 %) of AEs occurred during the dynamic stressing, whereas few AEs were released during static stress (Figure 4; Supplementary Material 1 Figures S6–S9); yet, the initial trends of released AEs varied widely between samples, especially when examining the AE release rates (which reached up to ~16,000 counts·min^{-1}). The AE release rates tended to increase with stress; however, in some cases, e.g. the hyaloclastite ash loaded to 20 MPa (Figure 4D), hyaloclastite lapilli loaded to 2 MPa (Supplementary Material 1 Figure S8A) and the scoria ash loaded to 5 and 10 MPa (Supplementary Material 1 Figure S7B, C) showed an initial reduction in AE release rate, before increasing with further loading. In the cases with scoria loaded to 20 MPa, we observe late-stage decreases in AEs beyond 10 MPa stress (Figure 4A, 4B). We observed no systematic differences in AE release rate evolution for samples with different grain sizes.

Upon initiation of creep under static stress, the AE rates dropped sharply to less than 5000 counts·min^{-1} within 40 min for all samples (Figure 4). As creep progressed, the AE release rates continued to reduce, ultimately reaching low rates which varied between lithologies and applied static stresses (Table 2). We observed that the AE release rates during late-stage creep generally positively correlate with the applied creep stress and strain rates experienced by the same sample; but for a few exceptions (e.g. the highest AEs of 417 counts·min^{-1} are found at 20 MPa for the hyaloclastite ash, which has a low strain rate of 4.01×10^{-8} s^{-1}; Table 2).

3.5 Grain size reduction during compaction

The compaction of volcaniclastic samples promoted grain size reduction with stressing for all experiments (Figure 5). A progressive reduction of larger grains and increase in smaller grains is observed under all applied stress conditions, indicating grain crushing even at the lowest stress condition of 2 MPa in all samples. Within each sample, all grain sizes increased in abundance in similar proportions; thus, the compaction and the resultant grain crushing produced grains of all sizes. Close examination of the data showed differences for the two lithologies and for the two different grain sizes. The abundance of the dominant (median) grain sizes of the lapilli (2.2 mm) were initially higher (at ~50–60 % of the population) than the dominant grain size (1.2 mm) in the ash (at ~25–30 %) and thus showed a greater reduction. The hyaloclastite compaction resulted in a greater production of fines (<0.125) than the scoria, at both ash and lapilli size, whereas the scoria grain size reduction was dominated by an increase in larger broken fragments (e.g. 1.7 mm in Figure 5A). In cases where we imparted creep after loading, we noted additional, yet trivial, reductions in grain size over the duration of the experiments (Supplementary Material 1 Figures S10–S11). The uncompacted samples were very monodisperse due to the sieving, as shown by a high polydispersivity index (Figure 6A). With compaction, samples became increasingly polydisperse, as shown by a decrease in the polydispersivity index during stressing (Figure 6A). The index reduction is

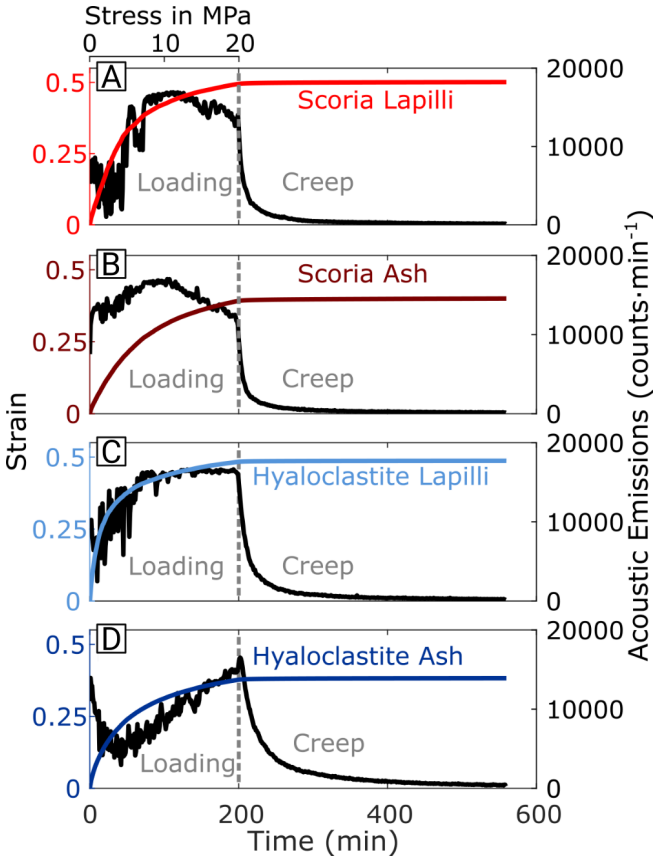

Figure 4: Acoustic emissions released during the dynamic and static stressing at 20 MPa for [A] scoria lapilli, [B] scoria ash, [C] hyaloclastite lapilli, and [D] hyaloclastite ash samples. Note the stress on the secondary axis during the loading phase. The plots show that most of the AEs occur during stressing, followed by a rapid reduction during the creep phase. The AEs obtained at other static stresses can be found in Supplementary Material 1 Figures S6–S9.

most significant at the start of stressing then the rate slows at higher stresses. Additional creep further reduces the polydispersivity index (Figure 6A), though in minor amounts (difference of 0.03 or less). Only the scoria ash under 2 MPa stress had a significant decrease in the polydispersivity index during creep (~0.05 difference). The scoria samples are less polydisperse than the hyaloclastites (higher index) but experience similar reductions in polydispersivity during compaction. Both ash samples are initially more polydisperse (lower index) than their lapilli counterparts, but they experience less significant reductions than the lapilli. This causes an initially less polydisperse hyaloclastite lapilli to become more polydisperse than the ash samples of both lithologies from 2 MPa onwards (Figure 6A).

3.6 Pre-compression stress and compression indices

To characterise the compression of granular samples, we assessed the evolution of void ratio (e) as a function of stress (Figure 6B). The void ratio decreased with applied stress, exhibiting an inflection (i.e. a shoulder) at a given stress (termed the pre-compression stress σ_P; see Figure 6B) beyond which the decrease in void ratio as a function of stress was more pronounced, as commonly observed in oedometer tests on soil [e.g. Mesri and Vardhanabhuti 2009]. The initial void ratio of both lapilli samples was higher than their ash counterparts, which can be attributed to the less efficient packing of the larger grains and the higher bulk porosity of the coarser assemblages. σ_P for the scoria was 0.93–1.13 MPa for the lapilli and 1.31–1.51 MPa for the ash, for the hyaloclastite σ_P was 0.20–0.28 MPa for the lapilli and 0.81–1.28 MPa for the ash. Lapilli samples experienced σ_P at lower stress than their ash counterparts for both lithologies (Figure 6B, 6C). σ_P is negatively correlated to the initial sample void ratio (Figure 6C), with the two lithologies indicating separate trends; the scoria has higher σ_P than hyaloclastite samples and shows a shallower slope with increasing void ratio compared to the hyaloclastites (Figure 6C). At stresses greater than σ_P, the slope of the void ratio as a function of stress (i.e. the primary compression index C_c calculated with Equation 9, indicated by the second tangent line in Figure 6B) was higher for the scoria than the hyaloclastite (Figure 6D). For both lithologies, C_c is correlated positively to the initial void ratio (Figure 6D), whereby the scoria has a stronger positive increase with void ratio compared to the hyaloclastites, though the offset is not as distinct as for σ_P. C_c was higher for the lapilli than for the ash for both lithologies, for the scoria it was 1.12–1.34 for the lapilli and 0.73–0.88 for the ash, and for the hyaloclastite C_c was 0.73–0.82 for lapilli and 0.60–0.62 for the ash. The quantified values of σ_P and C_c indicate that the hyaloclastites exhibited a lower threshold to compaction than the scoria, which in turn deformed at higher stresses. Results for σ_P and C_c are further summarised in Supplementary Material 1 Table S1.

The secondary compression index C_α (Table 2) was computed via Equation 10 for the last three hours of creep during the static stress tests. Using the methods in this study, C_α reflects essentially the same measurement of strain rate, hence the same overall trends can be observed (cf. Table 2). C_α was slightly higher for lapilli than ash at 10 MPa in the scoria and slightly lower than ash for all other samples, indicating only a minor impact of grain size compared to the lithology, where C_α was consistently higher in the scoria compared to the hyaloclastites across all stress conditions (by nearly an order of magnitude).

4 Interpretation

This experimental study revealed that volcaniclastic materials are variably impacted by dynamic and static stressing, and they exhibit different compaction behaviour depending on the material properties and the applied conditions. Under dynamic stressing, compaction was more pronounced during the onset of loading, then gradually slowed (Figure 2A, 2B) as has been noted during compaction of other volcaniclastic materials [Rotonda et al. 2010; Bai et al. 2023] and other granular materials such as sand [e.g. Karner et al. 2005; Ma et al. 2014]. Densification and reduction in bulk porosity was accompanied by extensive AEs (Figure 4) and a concomitant grain size reduction (Figure 5) with samples also becoming increasingly polydisperse (Figure 6A). The observed transient

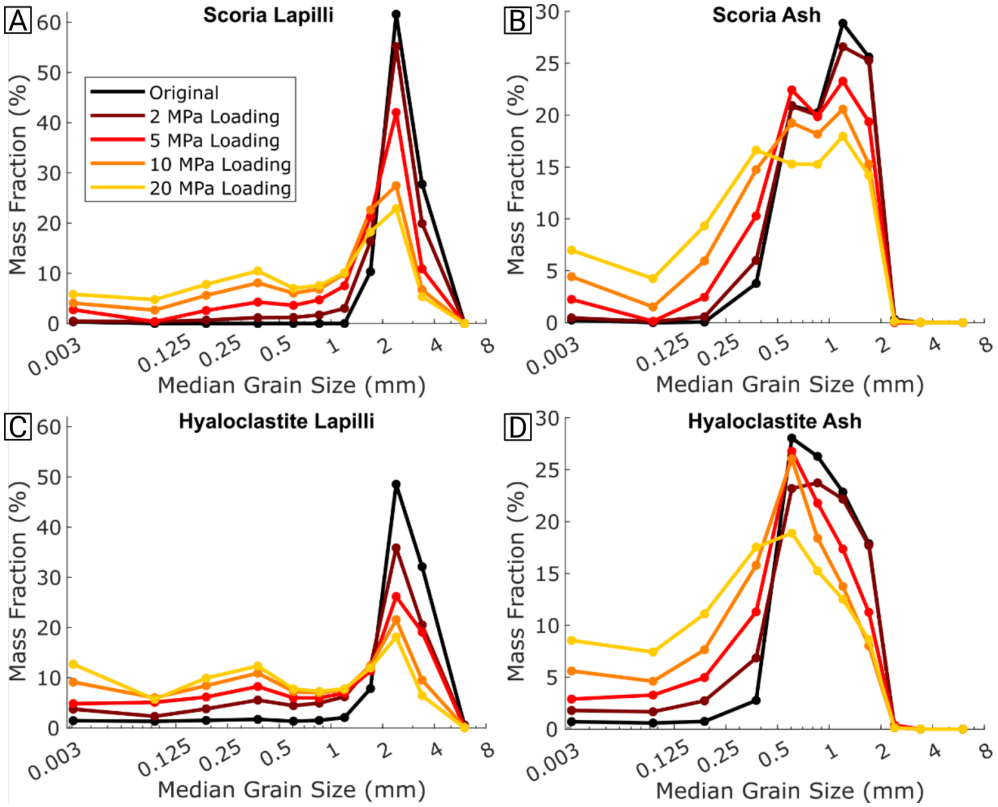

Figure 5: Grain size distributions of the original and post-experiment samples of [A] scoria lapilli, [B] scoria ash, [C] hyaloclastite lapilli, and [D] hyaloclastite ash samples obtained after dynamic stressing to 2, 5, 10, and 20 MPa, showing a systematic increase in finer grain size fractions at the expense of the larger ones as a function of applied stress. Here the grain size is shown as the median between two sieve sizes for one fraction. The grain sizes measured after the creep experiments only showed minor additional comminution and can be found in Supplementary Material 1 Figurse S10, S11.

behaviour reflects the reorganisation of grains during repacking of the volcaniclastic system and increasing comminution with applied stress [cf. Parkin 1991]. The contrasting original petrographic textures of our four samples permit an appraisal of lithological controls on compaction; i.e. rock type (scoria vs hyaloclastite) and grain size (lapilli vs ash). The compaction was sensitive to grain size, with the larger lapilli compressing more substantially than the ash for both the hyaloclastite and the scoria as it had initially higher inter-granular porosity and therefore more void space available for evolving packing (Figures 2–4). This is similar to results for compressing disaggregated sandstone, which showed that for samples with the same fragment size, total strain increased and total porosity decreased as a function of stress, and that under the same axial stress, the strain was higher with larger fragment size [Ma et al. 2014].

The pre-compression stress σ_P is generally interpreted to represent the threshold above which granular materials accumulate irreversible (inelastic) deformation [e.g. Dexter 1988; Horn and Lebert 1994]. In our experiments σ_P was 0.24–0.98 MPa for the hyaloclastite and 0.99–1.42 MPa for the scoria (Figure 6B, 6C), thus suggesting that strain is accommodated by reorganisation (rotation and sliding) without crushing at very low stresses in volcaniclastic systems, but, even the lowest target stress of 2 MPa used here resulted in both repacking and comminution (permanent changes). This is supported by acoustic emission release (Figure 4; Supplementary Material 1 Figures S6–S9) which increased with applied stress, and is an indicator of increased predominance of cracking events leading to damage accumulation [e.g. Kendrick et al. 2013]. The transition from grain sliding and rearrangement to grain crushing has been similarly evoked for the transition in behaviour of sand packs under increasing confining pressure [e.g. Karner et al. 2005]. The polydispersivity, packing density and contact friction also impact the stiffness and strength of the granular aggregates as more variably sized grains enable more grain connections (or stress chains), thereby better resisting compaction forces [Muthuswamy and Tordesillas 2006]. More connections also promote stronger bulk aggregates [Saadi et al. 2017]. In our data this increased polydispersivity during stressing (Figure 6A) is the likely cause of the observed decrease in deformation rate as samples compacted and densified (Figure 2A, 2D). However, this does not explain why the hyaloclastite is initially weaker than scoria, since it is also more polydisperse, suggesting inherent differences in particle stiffness as a result of the material's origin and genesis. The difference in the compaction behaviour of the scoria and hyaloclastite studied here can be attributed to their generation mechanism that produced contrasting textural characteristics; whilst the scoriaceous basalt results from vesiculation of a coherent lava, the indurated clasts of the hyaloclastite can be easily broken apart, leading to lower σ_P (Figure 6C). Earlier

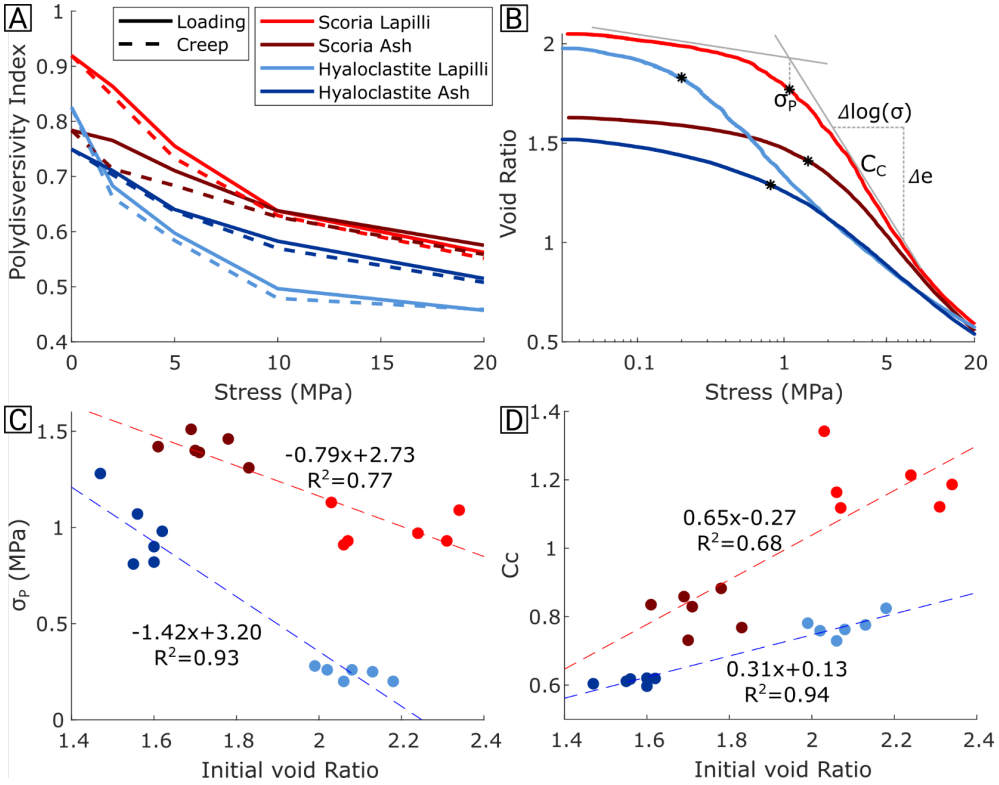

Figure 6: Evolution of volcaniclastics during stressing shown by the [A] polydispersivity index reducing with progressive compaction. Geomechanical parametrisation from [B] Oedometric compaction curves, showing the void ratio decrease with stress (here using the dynamic experiments up to 20 MPa, the oedometric compaction curves for all experiments can be found in Supplementary Material 1 Figure S4E–H). The initial void ratios of the individual samples are further compared against [C] pre-compression stresses σ_P and [D] the primary compression index C_c (excluding tests stressed at 2 MPa as the oedometric inflection was not sufficiently developed to make the measurements). Linear regressions are displayed for each lithology to highlight differences in trends, though more sample variation is needed to confirm and better constrain these.

work on intact hyaloclastite revealed failure by disaggregation at low stress [Eggertsson et al. 2020], seen here by the high production of fines (<0.125 mm) in the hyaloclastite (Figure 5C, 5D), whereas the post-deformation scoria samples are dominated by increased abundance of larger crushed grains that indicate grain splitting rather than disaggregation (Figure 5A, 5B). Indeed, stiff particles are more likely to experience grain splitting [Tang et al. 2001], and the scoria are likely to be stiffer and stronger than the hyaloclastites as pores are more rounded (Supplementary Material 1 Figure S2), with pore geometry having an important role in material strength [e.g. Baud et al. 2014].

In our static tests, applied stress was held over prolonged duration, resulting in progressive reduction in strain rate as expected for granular materials under constant load [Parkin 1991; Ma et al. 2014]. Strain rates were orders of magnitudes lower under static stress (Figure 3C–3F) as the material equilibrated to the applied conditions and compacted at a more steady rate (Table 2). AEs also reduced dramatically under static stress (especially in the first 15–30 minutes; Figure 4), relating to the non-linear time dependence of settlement of granular materials that starts rapidly and slows [Parkin 1991].

Comparing the compaction behaviour during dynamic versus static stressing, we found that compaction predominantly took place during dynamic loading. Because of the disparate amount of strain accommodated during dynamic stressing, the strain rates under static stress are difficult to interpret; the materials are already strained prior to creeping. Notably, during creep, the strain rates experienced by hyaloclastite were consistently lower (nearly an order of magnitude in most cases), likely due to the preferential initial comminution of the clasts in the hyaloclastite samples. There was however less difference in the creep behaviour as a function of grain size during the static stressing; as grain sizes primarily impacted compaction during the initial loading it may explain the negligible impact on compaction during creep, except at low static stresses where grain reorganisation did not complete during loading (Figure 3C–3F). Ultimately, we found that through compaction, volcaniclastic systems of contrasting grain sizes tended to establish similar behaviour via creep, despite retaining differences in grain size distribution (Figure 5). This may indicate that the residual pore space remains the key control on compaction of a given lithology.

We observed that creep generally had the highest strain rates at constant stresses of 5–10 MPa (Table 2). Acoustic emission rates during the last 30 minutes of creep at those stresses was also highest (Table 2), the only exception being the hyaloclastite at 20 MPa static stress, which exhibited low

strain rates despite a high AE rate. The fact that deformation is slower at both 2 and 20 MPa has different causes: at 2 MPa it is likely because the stress condition was hardly sufficient to induce damage (seen by the modest grain size reductions in Figure 5); at 20 MPa the samples were already significantly compacted and crushed, with the now more polydisperse pack being harder to deform further. This indicates that each volcaniclastic material would exhibit a distinct compaction signature based on its starting characteristics and loading history. We interpret that compaction creep of the porous volcaniclastic material would likely continue until it could no longer compact either by rearrangement or grain crushing under the applied stress, at a point which is likely to differ in terms of absolute strain or porosity reductions depending on the stress conditions.

5 Application to field scale

We used the controlled laboratory experiments to explore the surface expression of vertical ground deformation associated with the compaction of volcaniclastic systems. We considered a vertical column of confined, initially homogeneous, uncompressed material. As strain is controlled by applied stress, we explored the dependence of ground subsidence for deposits of variable initial thickness. We did this for two scenarios: a) near-instantaneous compaction (Figure 7), and b) time-dependent compaction (Figure 8).

Near-instantaneous compaction (loading): We discretised the deposit in depth, which had an initial direct relationship between the initial depth (z_0) and stress (σ):

$$\sigma = \rho_b g z_0, \tag{11}$$

using a simple lithostatic model with the compacted bulk density (ρ_b) and the gravitational acceleration (g). Using the measured strain (ε) as a function of stress, we integrated over the column to find the total equivalent deformation (subsidence) on the surface (SL) as a result of dynamic stressing (loading) for any given initial thickness (D):

$$SL\ (D) = \int_0^D \varepsilon(\sigma) dz_0. \tag{12}$$

Time-dependent compaction (creep): As ground deformation is commonly observed over prolonged periods in volcanic provinces, we modelled the creep deformation to make inferences about the potential role of volcaniclastic compaction for long-term flank creep at volcanoes. We first derived fitted analytical models for the strain rates ($\dot{\varepsilon}$) in the creep experiments (cf. Figure 3C–3F) as a function of both time (t) and stress (σ), which we fit using an empirical exponential power-law relationship:

$$\dot{\varepsilon}\ (t, \sigma) = e^{a(\sigma) \cdot t^{b(\sigma)} + c}, \tag{13}$$

where a and b are interdependent fitting parameters, that depend on both the sample and the static stresses, and which govern the reduction in strain rate with time. c is dependent on the initial creep strain rate at the end of the loading and is therefore very sensitive to the timing and sampling at the moment that loading ends. As a and b are also interdependent with c, allowing all three fitting parameters to vary made comparisons between different experiments difficult. After testing different fits, c was held fixed at a value of −5 which gives more consistent results for a and b. This reduced accuracy in the first minutes of creep, but maintained a better fit over longer timescales, with overall strains remaining similar between model and experiment data, making it suitable for geological observations.

The best-fit parameters for the creep experiments are listed in Supplementary Material 1 Figure S12A, S12B. We interpolated using a cubic spline for the dependency of these fit parameters on static stress (see Supplementary Material 1 Figure S12A, S12B) to apply the model to any given stress up to 20 MPa. We then integrated our solution through time to derive the total strain (ε) as a function of time (t_f) and stress (σ):

$$\varepsilon\ (t_f, \sigma) = \int_0^{t_f} \dot{\varepsilon}(t, \sigma) dt. \tag{14}$$

As above, we integrated over the initial column height. We maintained the coordinate system of the initial (uncompressed) column which is 1) evenly sampled in stress and unchanging with compression (same overburden) and 2) consistent with strain rates in the experimental data which were always relative to the initial sample height. We again integrated the creep strain to find the surface subsidence (SC):

$$SC(D) = \int_0^D \varepsilon\ (t_f, \sigma)\ dz_0. \tag{15}$$

We used this to calculate surface subsidence for specific initial deposit thicknesses and times, which enabled a prediction of deformation for volcaniclastic deposits (Figure 8).

Our models predict that most subsidence would occur near instantaneously upon deposition (Figure 7). A deposit thickness of 500 m would compact by ~120–180 m upon its emplacement, then continue to creep, but subsidence would be most significant in the first year (Figure 8). Here, the contrasting creep strain rate measurements between the scoria and hyaloclastite translate into significantly higher creep subsidence for the scoria; for instance, a 500 m-thick deposit of scoria could undergo up to ~10–15 m of ground subsidence due to compaction creep, whereas an equivalent deposit of hyaloclastite may experience a mere ~4–5 m within two years (Figures 7 and 8). While the given thickness was chosen to illustrate our results here, they are potentially realistic; for instance, the 1912 eruption of Novarupta (Valley of Ten Thousand Smokes) generated pyroclastic deposits up to 200 m thick within 16 hours [Fierstein and Wilson 2005], though most potential applications of our results will likely be considering smaller thicknesses. Our results also do not consider additional subsidence from cooling contraction of volcanic deposits, which will likely apply for pyroclastic deposits such as at Novarupta. For any given deposit thickness, most of this creep deformation would occur within around the first two days after emplacement, and through time deformation would progressively slow (Figure 8, Supplementary Material 1

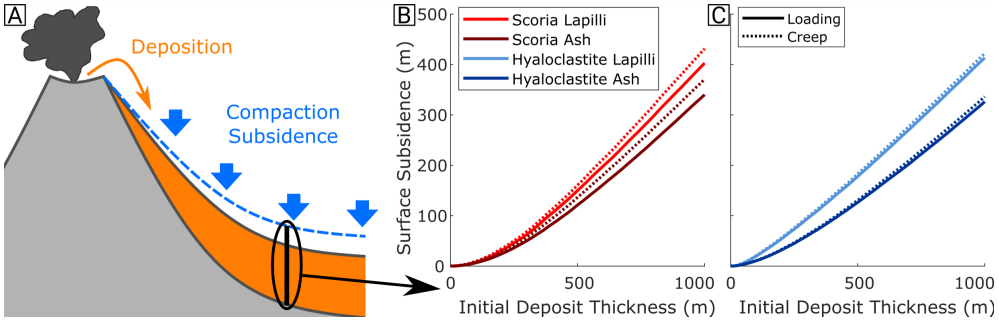

Figure 7: Compaction model for the tested materials assuming initially homogeneous deposits, showing [A] an illustration of new deposits emplaced on a flank that compact under their own weight, and the corresponding surface subsidence of [B] scoria and [C] hyaloclastite as a function of initial (uncompressed) deposit thickness. Solid lines indicate the expected compaction due to dynamic loading (near instantaneously) and the dashed lines mark the combined loading and creep deformation (here extrapolated to two years).

Figure S12C–F). We emphasise that these simulations hold for confined volcaniclastic deposits, but in the case where the materials could flow laterally, the ground subsidence may differ markedly. While only initially uncompacted materials were tested and modelled here, it is likely that similar timescales of creep would occur when stress conditions change. This may be by the deposition of new materials on top of existing units, thereby increasing static stress and starting a new period of creep under the changed stress conditions.

While these models for creep deformation are based on extrapolation of datasets acquired over a brief six-hour period, here we opt to validate the performance of the model forecast by comparing it with the creep deformation experiment conducted over around five days using the scoria lapilli sample (Supplementary Material 1 Figure S5). We found that the exponential power-law model generally appears as a good fit for the creep data. However, the extrapolation from six hours of creep tended to slightly underestimate the actual strain rates after five days (Supplementary Material 1 Figure S5). Hence, our results can be interpreted as a minimum expected subsidence due to creep.

6 Discussion

6.1 On the componentry of volcaniclastic systems

Volcaniclastic deposits are extremely diverse. Physically, they are made up of pyroclasts with different sizes, shapes and porosities of juvenile or lithic nature. Chemically and mineralogically, they encompass the full spectrum of volcanic products in fresh state (glassy or crystalline), but also altered following interaction with surrounding fluids. Volcanic rocks already exhibit a wide range of mechanical behaviour due to their variable porosity [see Heap and Violay 2021; Lavallée and Kendrick 2021 for reviews] thus volcaniclastic deposits of heterogeneous clasts are likely to have an even broader spectrum of mechanical behaviours.

During deformation of volcaniclastics progressive rearrangement and changes in grain size distribution by grains breaking and crushing as observed in our experiments impact the compaction dynamics. The different constituent phases of volcaniclastics consisting of primary minerals (plagioclase, pyroxene, quartz, etc.), pores, glass and secondary phases (e.g. phyllosilicates, clays, zeolites), have highly contrasting strength and, thus, compaction behaviour will differ for each lithology. The hyaloclastite contains alteration minerals, mainly zeolites and smectites [Eggertsson et al. 2020; Weaver et al. 2020], which easily deform and shed as a fine powder, which may reduce inter-grain friction and shear strength [e.g. del Potro and Hürlimann 2009]. These alteration minerals in a granular mixture may facilitate grain mobility and reduce particle interlocking, enabling disaggregation and efficient compaction [e.g. Won et al. 2023]. Similarly, the shape of grains influences the compressibility of volcaniclastic systems, with packs of rounded clasts likely to be stiffer [Koutous and Hilali 2019] and spherical grains likely to be stronger than irregular ones [Tang et al. 2001]. Moreover grain size reduction depends on grain shape, as irregular grains are particularly prone to crushing rather than splitting which tends to dominate in dense, regular shaped grains [Tang et al. 2001]. Our experiments were done on crushed volcanic rocks with highly irregular shapes, representative of primary volcaniclastic deposits (pyroclastic fallout deposits, or breccias), but perhaps not of far-reaching pyroclastic density currents or secondary (reworked) volcanic deposits (e.g. lahar deposits), which may contain more rounded clasts (due to transport comminution). Depending on particle size, mineralogy, and ambient conditions (dry vs wet), volcaniclastic systems exhibit variable degrees of cohesion [Walding et al. 2023]. Dry uncompressed ash and lapilli (as used in our experiments) have practically no cohesion but upon compaction and grain crushing, it is possible that the system would acquire some degree of cohesion due to increasing polydispersivity and interlocking. Similarly, the presence of moisture or water can drastically increase the cohesion [Walding et al. 2023] and modify the mechanical properties of particulate materials [e.g. Nawaz et al. 2013; Kodikara et al. 2018] particularly if clay alteration products are present [e.g. Dafalla 2013]. These mineralogy-, size- and environment-dependent constraints should be investigated systematically in future mechanical studies on volcaniclastic systems.

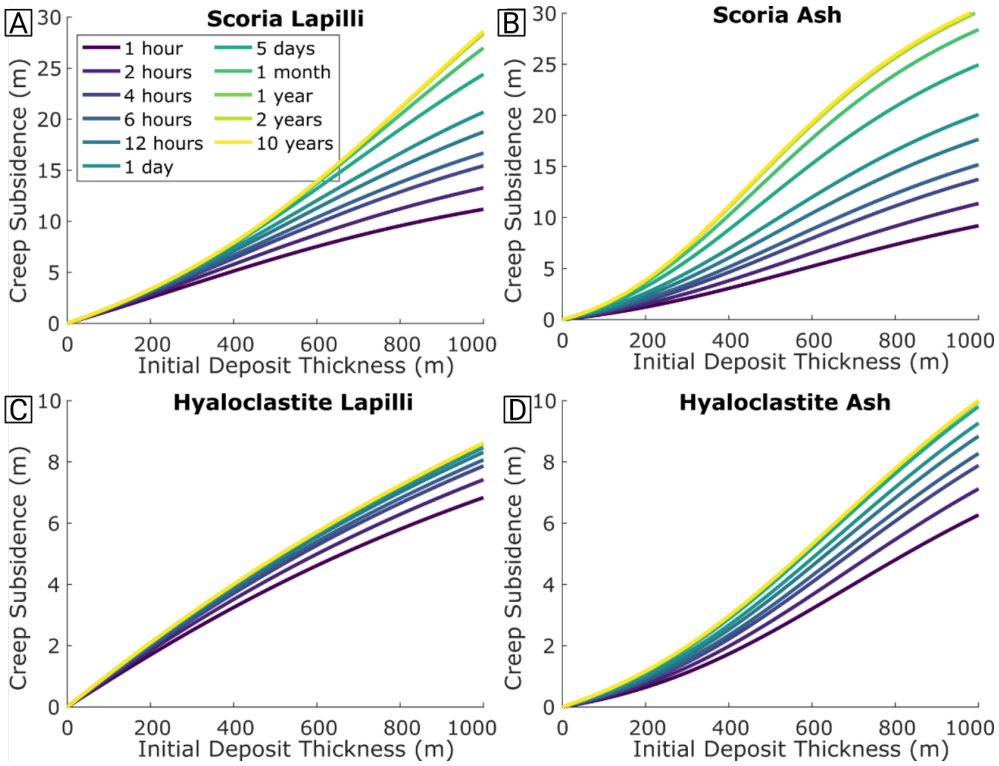

Figure 8: Model prediction for surface subsidence over time due to creep compaction for the [A] scoria lapilli, [B] scoria ash, [C] hyaloclastite lapilli, and [D] hyaloclastite ash. Overlapping lines from 1, 2, and 10 years suggest that creep becomes insignificant after less than one year for all deposits and thicknesses.

6.2 Compaction behaviour of volcaniclastic materials vs other clastic systems

The two types of compaction experiments conducted herein demonstrate the influence of lithology, grain size, and stress on the progression of compaction. This is in agreement with recent assessments made by Schaefer et al. [2023], who determined bulk porosity (influenced by grain size distribution) and lithology as primary parameters impacting the mechanical behaviour of variably altered scoria. Our findings indicate that the initial grain size distribution (and/or bulk porosity) of volcaniclastics primarily governs strain accumulated during compaction, whereas the clast type (dense, vesicular, agglutinated, monomineralic) influences damage accumulation (e.g. comminution/ rupture). The porosity of clasts influences strength and so, plays a significant role on their ability to comminute, fracture, and crush [see Wong and Baud 2012; Baud et al. 2014; Lavallée and Kendrick 2021 and references therein], thus impacting the compaction of a deposit.

The porosity of pyroclasts in volcaniclastic deposits sets them apart from other clastic systems (e.g. sands or soils) and consequently the compaction of our samples differs drastically from that of dense quartz sand [e.g. Parkin 1991; Hagin and Zoback 2004; Karner et al. 2005; Ma et al. 2014], even if they hold similar initial void ratios [e.g. Mesri and Vardhanabhuti 2009]. For instance, quartz sand has been observed to accumulate damage only once it experiences pre-compression stresses exceeding ~15–30 MPa [cf. Mesri and Vardhanabhuti 2009], whereas even at our lowest tested condition of 2 MPa we induced grain size reduction. Hence, porous volcaniclastic samples are susceptible to deform under much lower stresses than sand and other clastic systems made of dense clasts (notwithstanding other variables, e.g. the addition of micas [Mesri and Vardhanabhuti 2009]). For such (non-volcanic) clastic materials containing dense grains, it has been demonstrated that the pre-compression stress σ_P and the compressive index C_c of a given system respectively correlate negatively and positively with the initial uncompressed void ratio [Keller et al. 2011; Won et al. 2023], making it a robust metric to model compaction. Our data supports this and demonstrated that the same general trends apply to volcaniclastic materials. In our experiments σ_P reduces with increasing void ratio (here resulting from larger grain size, lapilli vs ash), and C_c increases with void ratio (Figure 6B–6D), as in other materials [Keller et al. 2011; Won et al. 2023]. Dense grain aggregates generally have lower void ratios (0.5–1.3), lower C_c (0.1–0.5) and higher σ_P (15–100 MPa) (cf. Figure 6C, 6D; Keller et al. [2011]). But by extrapolating these trends to higher void ratios such as measured in our volcaniclastic aggregates, C_c in particular shows good agreement, indicating that void ratio has the dominant control on the primary compressive index. However, the two types of volcaniclastic lithics exhibit distinct trends, particularly for σ_P as a function of void ratio (Figure 6C, 6D), which can likely be attributed to their mineralogy and texture. The scoria has higher solid density and comprises large round vesicles in a dense groundmass with rare phenocrysts. The hyaloclastite is made of agglutinated glassy, micro-vesicular basalt fragments with abundant phenocrysts, and these fragments are coated with alteration products. These differences result

in a lower σ_P and C_c for the hyaloclastite than the scoria. Given the much higher σ_P measured for quartz sand (comprised of strong mono-mineralic grains [Keller et al. 2011]), we speculate that the clast strength can result in a vertical offset of the negative trend of σ_P with void ratio, supported by the agglutinated clastic nature of the hyaloclastite which is prone to disaggregation even at low stresses, which may be considered weaker than the scoria with higher σ_P.

Axial compaction experiments on volcaniclastic systems using a rigid cup (oedometer-type experiments) were also performed by Bai et al. [2023] on scoria samples from Hongtu Hill, China. They showed that grain size reduction is proportional to the applied stress, as observed herein. The reduction in porosity was largest during the early loading (up to 10 MPa) and then slowed, in agreement with our experiments; however, as they reached greater stresses than we did, they observed further increases in compaction rates between 50 and 70 MPa [Bai et al. 2023]. They attribute these two phases of porosity reduction to grain repacking in the early phase and grain crushing at higher stresses; yet, as we monitored AEs during our experiments and measured the grain size distribution of our experimental products, we observed that grain comminution is already prevalent at stresses as low as 2 MPa. Bai et al. [2023] also observed the formation of compaction bands within the sample at stresses as low as 10 MPa, which is attributed to the high grain porosity of volcanic deposits forming natural weak zones. We could not observe these features in our experiments (as we used an opaque metal cylinder as confinement) but we anticipate that they may have formed in the samples.

Volcaniclastic material rheology was also experimentally investigated for deposits from Stromboli volcano, Italy [Boldini et al. 2009; Rotonda et al. 2010]. While they focused mostly on the shear and frictional properties of the material, some oedometer compaction experiments were also performed at stresses up to 1.6 MPa [Rotonda et al. 2010]. They observed time-dependent creep strain, with initially high strain and strain rates, which non-linearly reduced too rapidly to establish a near-linear accumulation of strain at a slow compression rate. Notably, our most similar sample (the scoria) exhibited contrasting indices of secondary compression C_α; 0.0161 (lapilli) and 0.0187 (ash) at 2 MPa in our experiments as opposed to 0.0019 at 1.6 MPa in Rotonda et al. [2010], implying that the Stromboli pyroclastic system tested was more resistant to compression. We postulate that this may reflect the more varied nature of the sample tested in terms of grain size distribution (polydisperse), which would prevent extensive repacking. Using their observation, Rotonda et al. [2010] suggested that the prolonged, vertical ground motion measured at Stromboli by Baldi et al. [2008] may reflect the compaction of volcaniclastic deposits undergoing gradual grain crushing. Our combined AE and time-dependent creep deformation datasets, obtained over a broader stress range than Rotonda et al. [2010], support this hypothesis. However, the low stresses used to test sample creep in Rotonda et al. [2010] are barely above the pre-compression stress in our data, which likely hindered effective creep. This may also explain their much lower C_α as our tests constrained C_α at higher static stresses of 5 and 10 MPa.

6.3 Implications for volcanic flank instability

Volcanic flank instability is a prevalent issue in volcanic provinces, as evidenced by sector collapse deposits and collapse scars in the geologic record [Kerr 1984; Siebert 1992] and by monitored ground deformation data [Borgia et al. 1992; Poland et al. 2017; Schaefer et al. 2019]. The lack of knowledge and quantitative description of the mechanical properties of volcaniclastic lithologies remains a major hindrance to our deformation models and the assessment of volcanic mass-movement hazards. Here, we have shown that volcaniclastic material compresses significantly under low stresses, even from minor burial associated with the emplacement of overlying materials due to prolonged accumulation or later renewed volcanic activity. The experiments demonstrated that the type of lithology, the grain size, the overburden stress, and the duration of stressing are primary controls on compaction. We make inferences about the potential role of volcaniclastic compaction in different case examples of volcano edifice construction, deformation, and flank collapse:

(1) Volumetric compaction is substantial at shallow burial depths, such that 100 m-thick deposits may exhibit 6–20 m of ground subsidence (Figure 7). Such a thickness can easily be accumulated during a single eruption; for instance, the 2021 Tajogaite eruption on Cumbre Vieja volcano (La Palma) built a 110 m high scoria cone within just 8 days and nearly 190 m by the end of the eruption after 85 days [Bonadonna et al. 2022; Civico et al. 2022]. Thus, compaction and changes in material properties are anticipated to be substantial and significantly impact the structural stability of the deposits.

(2) The high sensitivity of volcaniclastic samples to compaction (particularly under low stresses) suggests that rapid changes in overburden or effective stress may trigger ground subsidence (even of deposits in the subsurface). This may explain the occurrence of sudden flank movements at volcanoes experiencing changes in local stress (via burial, pore fluid pressure fluctuations, tectonic activity, etc.). One such example may have occurred at Pacaya volcano, Guatemala, where the flank of the upper edifice underwent a sudden slump during the 2010 eruption and had deformation persisting for several months [Schaefer et al. 2016]. This was hypothesised to be caused by compaction of volcaniclastic materials in the lower flank [Schaefer et al. 2016], and we ponder whether the deposition of new lava at the summit added weight to trigger rapid compaction and, in turn, partial collapse; although other causes (e.g. changes in pore fluid pressure as a result of magma intrusion) cannot be ruled out. The prolonged ground subsidence reported during May 2010 and April 2014 at Pacaya [Schaefer et al. 2016] may indicate the action of creep deformation as constrained in our study (Figure 8).

(3) Our experimental setup indicates that in volcaniclastic deposits, compaction creep operates to a significant level for relatively short periods of time—arguably, up to some months, but primarily within the first few days. Such short timescales

and, in turn, insubstantial amounts of deformation at longer timescales make satellite-based (e.g. InSAR) ground deformation measurement at volcanoes challenging because it presents a narrow observation window. In addition, as regular eruptive activity and deposition of new materials may be ongoing, compaction may carry on variably, thus contributing to other sources of ground deformation. For instance, ground deformation observed on the southwest flank of Anak Krakatau, Indonesia, prior to its collapse in December 2018, was concurrent with the regular accumulation of eruptive scoria and ash; however, it remains as yet impossible to ascertain whether volcaniclastic compaction contributed to the deformation associated with frictional sliding of the flank ultimately observed [Zorn et al. 2023]. Magnitudes and timescales of ground deformation may be particularly helpful here, as compaction in our data is expected to encompass centimeter- to metercale subsidence in days to months depending on thickness, whereas, e.g. thermal cooling has been observed in scales of millimeters per year to centimeters per year after 5–15 years [Wittmann et al. 2017], degassing and crystallisation of magma reservoirs in scales of centimeters per year lasting a few years [Caricchi et al. 2014], or volcano flank instability [Poland et al. 2017] in scales of centimeters per year lasting decades. Here, an improved understanding of volcaniclastic compaction may eventually enable such distinctions to constrain more accurate models of volcano deformation and structural instability.

(4) Compaction is accompanied by reductions in bulk porosity and void ratio, and increases in the bulk density, resulting in depth-dependent changes in the physical and mechanical properties of the materials involved. These variables are key parameters used to model volcanic edifices' structural stability [e.g. Schaefer et al. 2015]. Additionally, compaction would reduce fluid storage capacity and permeability [e.g. Ashwell and Kendrick et al. 2015; Wadsworth et al. 2016], which may promote pore fluid pressurisation [e.g. Farquharson et al. 2017] that may prompt volcano instability [Day 1996]. For example, pore fluid pressurisation due to the shallow intrusion of a cryptodome in a volcanic edifice was hypothesised to have been a major factor in the lateral collapses of Mount St. Helens, USA, in 1980, and of Bezymianny, Russia, in 1956 [Donnadieu et al. 2001].

Experimental investigations are key to obtain robust, quantitative descriptions of geomaterials' behaviour; yet, application of the findings to natural processes (as undertaken with our empirical models) should always be done with caution as inferences are inherently associated with limitations and assumptions, some of which are addressed here. Our investigation uses natural volcaniclastic materials, which facilitates applicability; however, as we tested a narrow range of sample characteristics (density, porosity, mineralogy, grain sizes, and polydispersivity) the observations are unlikely to fully capture the breadth of deformation behaviour anticipated in volcanic deposits, which have complex litho-stratigraphic heterogeneity. We opted for the methods employed herein, as they allowed us to track porosity and density evolution during compaction, however, we could not measure inter-granular friction or cohesion, which are known to play key roles in volcaniclastic systems [e.g. Vandewalle et al. 2007; Lavallée and Kendrick 2021; Walding et al. 2023]. Also, the selected stressing rate of 0.1 MPa may limit applicability to scenarios in which burial rates would be much slower or faster, possibly by several orders of magnitude. Moreover, the short creep duration makes extrapolation to the deformation timescales commonly monitored at volcanoes (weeks to years) rather challenging. Finally, the use of a rigid container would make the application of our findings realistic to volcaniclastic deposits emplaced within the confines of depressions (e.g. valleys, calderas, etc.) and surrounded by strong, dense lavas, or surrounded by granular material undergoing the same degree of compaction as they would deform "vertically", whereas partially confined deposits on steep volcanic flanks may flow laterally. Yet, here, we hope that the findings of this study will help to shed new light on the role of structural instability of surficial or shallow volcaniclastic systems at deforming volcanoes and in turn, promote future studies to systematically describe volcaniclastic rheology and bridge some of the aforementioned gaps to improve our understanding of gravitational compaction of volcaniclastic deposits.

While the tested dataset used to model the instantaneous and time-dependent deformation is limited to two lithologies and two grain sizes, in a dry ambient environment, the results highlight the fundamental importance of volcaniclastic systems in ground deformation models to improve hazard assessment efforts. Volcaniclastic deposits are extremely diverse so we encourage further field and experimental studies aiming to constrain the full spectrum of deformation behaviour under a wider range of ambient conditions extant in volcaniclastic provinces.

7 Conclusions

We experimentally investigated the compaction of four different volcaniclastic materials (scoria and hyaloclastite of ash and lapilli grain size via 1) dynamic and 2) static stressing. We monitored length change and acoustic emissions and observed that volcaniclastic materials may compact rapidly, leading to substantial strain, porosity reduction and densification. Compaction mostly occurred during loading, especially at low stresses where the resultant strain rates were highest; then the compaction rates reduced with stress as samples densified. AEs associated with a combination of grain repacking and comminution increased with stress. The lapilli samples compacted more significantly during early loading (due to the lower packing efficiency of larger grains), thus accumulating higher total strains than ash samples, however, the compaction behaviour of lapilli and ash converged at higher stresses as the volcaniclastic systems achieved similar bulk density, bulk porosity, and void ratio through compaction, grain packing and comminution. Comparing between the behaviour of different lithologies, we observed that the weaker hyaloclastites initially (within the first ~2 MPa) compacted faster than the scoria, but then slowed more significantly at higher stresses, which we attribute to their contrasting textural characteristics.

The samples all underwent compaction creep under prolonged applied stresses. During creep, strain rates rapidly

declined after reaching the target static stress, with scoria exhibiting consistently higher strain rates than the hyaloclastites. For all tested samples, the creep strain rates were highest at 5–10 MPa applied stress; lower stress was insufficient to promote extensive compaction and at higher stress the dynamic loading had already efficiently compacted the system. As such, compaction dominantly occurs during dynamic stressing, and in volcaniclastic systems are likely to exhibit prolonged creep deformation when buried between ~400–1200 m.

The instantaneous and time-dependent compaction of volcaniclastic deposits, during dynamic loading (upon burial) and static stress hold (i.e. prolonged creep) respectively, may promote significant deformation at volcanoes. We observed that a mere 2 MPa of applied stress (commensurate with a burial of depth or thickness of ~180–230 m) caused volcaniclastic compaction to reach 10–30 vol.% or an equivalent surface subsidence of 24–55 m. Prolonged creep can be expected to add another ~1–3 m subsidence within less than a year, with the majority of this deformation occurring within the first days after burial.

We found the compaction behaviour of porous volcaniclastic materials differs significantly from that of soils or dense granular materials, on which the majority of work to date has focussed, which emphasises the need to increase our attention on volcaniclastics to improve our interpretation of ground deformation signals at volcanoes in order to improve our assessment of flank instabilities and engineer risk-mitigation countermeasures.

Author Contributions

This study was conceptualised by EUZ, JEK, AL and YL. All laboratory measurements and experiments were conducted by EUZ, JEK, AL and UK and data was analysed EUZ, JEK, AL and YL. BSE imaging was performed by MMS and EUZ and data fitting and extrapolation were conceptualised and performed by JB and EUZ. Figures were prepared by EUZ. All authors contributed to the writing of the manuscript.

Acknowledgements

We acknowledge financial support from the European Research Council (ERC) for a consolidator grant on Magma Outgassing During Eruptions and Geothermal Exploration (MODERATE No.101001065), and a research grant of the Natural Environment Research Council (NERC) on Transient magma permeability and gas flow: a combined experimental and theoretical model (NE/T007796/1). We also acknowledge support from the LMUexcellent, funded by the Federal Ministry of Education and Research (BMBF) and the Free State of Bavaria under the Excellence Strategy of the Federal Government and the Länder.

Data Availability

The compaction data used in this study are provided via Zenodo at https://doi.org/10.5281/zenodo.14186062. All other data are available in the paper or in the accompanying Supplementary Material file.

Copyright Notice

References

Ashwell, P. A., J. E. Kendrick, Y. Lavallée, B. M. Kennedy, K.-U. Hess, F. W. von Aulock, F. B. Wadsworth, J. Vasseur, and D. B. Dingwell (2015). "Permeability of compacting porous lavas". *Journal of Geophysical Research: Solid Earth* 120(3), pages 1605–1622. DOI: 10.1002/2014jb011519.

Augustesen, A., M. Liingaard, and P. V. Lade (2004). "Evaluation of Time-Dependent Behavior of Soils". *International Journal of Geomechanics* 4(3), pages 137–156. DOI: 10.1061/(asce)1532-3641(2004)4:3(137).

Bai, J., H. Tang, J. Hu, L. Yang, T. Guo, and Z. Zhang (2023). "Characteristics and Controlling Factors of Particle Crushing in Volcaniclastic Sediments under Compaction: The Quaternary Pyroclastic Deposits of Hongtu Hill, Changbaishan Area, Northeastern China". *Minerals* 13(10), page 1351. DOI: 10.3390/min13101351.

Baldi, P., M. Coltelli, M. Fabris, M. Marsella, and P. Tommasi (2008). "High precision photogrammetry for monitoring the evolution of the NW flank of Stromboli volcano during and after the 2002–2003 eruption". *Bulletin of Volcanology* 70(6), pages 703–715. DOI: 10.1007/s00445-007-0162-1.

Baud, P., T.-F. Wong, and W. Zhu (2014). "Effects of porosity and crack density on the compressive strength of rocks". *International Journal of Rock Mechanics and Mining Sciences* 67, pages 202–211. DOI: 10.1016/j.ijrmms.2013.08.031.

Boldini, D., F. Wang, K. Sassa, and P. Tommasi (2009). "Application of large-scale ring shear tests to the analysis of tsunamigenic landslides at the Stromboli volcano, Italy". *Landslides* 6(3), pages 231–240. DOI: 10.1007/s10346-009-0155-6.

Bonadonna, C., M. Pistolesi, S. Biass, M. Voloschina, J. Romero, D. Coppola, A. Folch, L. D'Auria, A. Martin-Lorenzo, L. Dominguez, C. Pastore, M.-P. Reyes Hardy, and F. Rodríguez (2022). "Physical Characterization of Long-Lasting Hybrid Eruptions: The 2021 Tajogaite Eruption of Cumbre Vieja (La Palma, Canary Islands)". *Journal of Geophysical Research: Solid Earth* 127(11). DOI: 10.1029/2022jb025302.

Borgia, A., L. Ferrari, and G. Pasquarè (1992). "Importance of gravitational spreading in the tectonic and volcanic evolution of Mount Etna". *Nature* 357(6375), pages 231–235. DOI: 10.1038/357231a0.

Caricchi, L., J. Biggs, C. Annen, and S. Ebmeier (2014). "The influence of cooling, crystallisation and re-melting on the interpretation of geodetic signals in volcanic systems". *Earth and Planetary Science Letters* 388, pages 166–174. DOI: 10.1016/j.epsl.2013.12.002.

Castagna, A., A. Ougier-Simonin, P. M. Benson, J. Browning, R. J. Walker, M. Fazio, and S. Vinciguerra (2018). "Ther-

mal Damage and Pore Pressure Effects of the Brittle-Ductile Transition in Comiso Limestone". *Journal of Geophysical Research: Solid Earth* 123(9), pages 7644–7660. DOI: 10.1029/2017jb015105.

Chen, Y., D. Remy, J.-L. Froger, A. Peltier, N. Villeneuve, J. Darrozes, H. Perfettini, and S. Bonvalot (2017). "Long-term ground displacement observations using InSAR and GNSS at Piton de la Fournaise volcano between 2009 and 2014". *Remote Sensing of Environment* 194, pages 230–247. DOI: 10.1016/j.rse.2017.03.038.

Cigala, V., U. Kueppers, J. J. Peña Fernández, J. Taddeucci, J. Sesterhenn, and D. B. Dingwell (2017). "The dynamics of volcanic jets: Temporal evolution of particles exit velocity from shock-tube experiments". *Journal of Geophysical Research: Solid Earth* 122(8), pages 6031–6045. DOI: 10.1002/2017jb014149.

Civico, R., T. Ricci, P. Scarlato, J. Taddeucci, D. Andronico, E. Del Bello, L. D'Auria, P. A. Hernández, and N. M. Pérez (2022). "High-resolution Digital Surface Model of the 2021 eruption deposit of Cumbre Vieja volcano, La Palma, Spain". *Scientific Data* 9(1). DOI: 10.1038/s41597-022-01551-8.

Dafalla, M. A. (2013). "Effects of Clay and Moisture Content on Direct Shear Tests for Clay-Sand Mixtures". *Advances in Materials Science and Engineering* 2013, pages 1–8. DOI: 10.1155/2013/562726.

Day, S. J. (1996). "Hydrothermal pore fluid pressure and the stability of porous, permeable volcanoes". *Geological Society, London, Special Publications* 110(1), pages 77–93. DOI: 10.1144/gsl.sp.1996.110.01.06.

Del Potro, R. and M. Hürlimann (2009). "The decrease in the shear strength of volcanic materials with argillic hydrothermal alteration, insights from the summit region of Teide stratovolcano, Tenerife". *Engineering Geology* 104(1–2), pages 135–143. DOI: 10.1016/j.enggeo.2008.09.005.

Dexter, A. (1988). "Advances in characterization of soil structure". *Soil and Tillage Research* 11(3–4), pages 199–238. DOI: 10.1016/0167-1987(88)90002-5.

Donnadieu, F., O. Merle, and J.-C. Besson (2001). "Volcanic edifice stability during cryptodome intrusion". *Bulletin of Volcanology* 63(1), pages 61–72. DOI: 10.1007/s004450000122.

Douillet, G. A., K. R. Rasmussen, U. Kueppers, D. Lo Castro, J. P. Merrison, J. J. Iversen, and D. B. Dingwell (2014). "Saltation threshold for pyroclasts at various bedslopes: Wind tunnel measurements". *Journal of Volcanology and Geothermal Research* 278–279, pages 14–24. DOI: 10.1016/j.jvolgeores.2014.03.011.

Eggertsson, G. H., J. E. Kendrick, J. Weaver, P. A. Wallace, J. E. P. Utley, J. D. Bedford, M. J. Allen, S. H. Markússon, R. H. Worden, D. R. Faulkner, and Y. Lavallée (2020). "Compaction of Hyaloclastite from the Active Geothermal System at Krafla Volcano, Iceland". *Geofluids* 2020, pages 1–17. DOI: 10.1155/2020/3878503.

Farquharson, J. I., P. Baud, and M. J. Heap (2017). "Inelastic compaction and permeability evolution in volcanic rock". *Solid Earth* 8(2), pages 561–581. DOI: 10.5194/se-8-561-2017.

Fierstein, J. and C. J. Wilson (2005). "Assembling an ignimbrite: Compositionally defined eruptive packages in the 1912 Valley of Ten Thousand Smokes ignimbrite, Alaska". *Geological Society of America Bulletin* 117(7), page 1094. DOI: 10.1130/b25621.1.

Gottsmann, J., E. Eiden, and M. E. Pritchard (2022). "Transcrustal Compressible Fluid Flow Explains the Altiplano-Puna Gravity and Deformation Anomalies". *Geophysical Research Letters* 49(16). DOI: 10.1029/2022gl099487.

Hagin, P. N. and M. D. Zoback (2004). "Viscous deformation of unconsolidated reservoir sands—Part 1: Time-dependent deformation, frequency dispersion, and attenuation". *Geophysics* 69(3), pages 731–741. DOI: 10.1190/1.1759459.

Heap, M. J., J. I. Farquharson, P. Baud, Y. Lavallée, and T. Reuschlé (2015). "Fracture and compaction of andesite in a volcanic edifice". *Bulletin of Volcanology* 77(6). DOI: 10.1007/s00445-015-0938-7.

Heap, M. J. and M. E. Violay (2021). "The mechanical behaviour and failure modes of volcanic rocks: a review". *Bulletin of Volcanology* 83(5). DOI: 10.1007/s00445-021-01447-2.

Horn, R. and M. Lebert (1994). "Soil Compactability and Compressibility". *Soil Compaction in Crop Production*. Elsevier, pages 45–69. DOI: 10.1016/b978-0-444-88286-8.50011-8.

Hornby, A., U. Kueppers, B. Maurer, C. Poetsch, and D. Dingwell (2020). "Experimental constraints on volcanic ash generation and clast morphometrics in pyroclastic density currents and granular flows". *Volcanica* 3(2), pages 263–283. DOI: 10.30909/vol.03.02.263283.

Karner, S. L., J. S. Chester, F. M. Chester, A. K. Kronenberg, and A. Hajash (2005). "Laboratory deformation of granular quartz sand: Implications for the burial of clastic rocks". *AAPG Bulletin* 89(5), pages 603–625. DOI: 10.1306/12200404010.

Keller, T., M. Lamandé, P. Schjønning, and A. R. Dexter (2011). "Analysis of soil compression curves from uniaxial confined compression tests". *Geoderma* 163(1–2), pages 13–23. DOI: 10.1016/j.geoderma.2011.02.006.

Kendrick, J. E., Y. Lavallée, N. R. Varley, F. B. Wadsworth, O. D. Lamb, and J. Vasseur (2016). "Blowing Off Steam: Tuffisite Formation As a Regulator for Lava Dome Eruptions". *Frontiers in Earth Science* 4. DOI: 10.3389/feart.2016.00041.

Kendrick, J. E., R. Smith, P. Sammonds, P. G. Meredith, M. Dainty, and J. S. Pallister (2013). "The influence of thermal and cyclic stressing on the strength of rocks from Mount St. Helens, Washington". *Bulletin of Volcanology* 75(7). DOI: 10.1007/s00445-013-0728-z.

Kerr, R. A. (1984). "Landslides from Volcanoes Seen as Common: Given the example of Mount St. Helens' catastrophic collapse, geologists are recognizing volcanic debris avalanches elsewhere". *Science* 224(4646), pages 275–276. DOI: 10.1126/science.224.4646.275.

Kodikara, J., T. Islam, and A. Sounthararajah (2018). "Review of soil compaction: History and recent developments". *Transportation Geotechnics* 17, pages 24–34. DOI: 10.1016/j.trgeo.2018.09.006.

Koutous, A. and E. Hilali (2019). "Grain shape effects on the mechanical behavior of compacted earth". *Case Studies in Construction Materials* 11, e00303. DOI: 10.1016/j.cscm.2019.e00303.

Kueppers, U., C. Putz, O. Spieler, and D. B. Dingwell (2012). "Abrasion in pyroclastic density currents: Insights from tumbling experiments". *Physics and Chemistry of the Earth, Parts A/B/C* 45–46, pages 33–39. DOI: 10.1016/j.pce.2011.09.002.

Lavallée, Y., T. Hirose, J. E. Kendrick, S. De Angelis, L. Petrakova, A. J. Hornby, and D. B. Dingwell (2014). "A frictional law for volcanic ash gouge". *Earth and Planetary Science Letters* 400, pages 177–183. DOI: 10.1016/j.epsl.2014.05.023.

Lavallée, Y. and J. E. Kendrick (2021). "A review of the physical and mechanical properties of volcanic rocks and magmas in the brittle and ductile regimes". *Forecasting and Planning for Volcanic Hazards, Risks, and Disasters*. Elsevier, pages 153–238. ISBN: 9780128180822. DOI: 10.1016/b978-0-12-818082-2.00005-6.

Ma, Z., R. Gu, Z. Huang, G. Peng, L. Zhang, and D. Ma (2014). "Experimental study on creep behavior of saturated disaggregated sandstone". *International Journal of Rock Mechanics and Mining Sciences* 66, pages 76–83. DOI: 10.1016/j.ijrmms.2014.01.004.

Mesri, G. and B. Vardhanabhuti (2009). "Compression of granular materials". *Canadian Geotechnical Journal* 46(4), pages 369–392. DOI: 10.1139/t08-123.

Monkul, M. M. and G. Ozden (2007). "Compressional behavior of clayey sand and transition fines content". *Engineering Geology* 89(3–4), pages 195–205. DOI: 10.1016/j.enggeo.2006.10.001.

Moore, P. L., N. R. Iverson, and R. M. Iverson (2008). *Frictional properties of the Mount St. Helens gouge*. Edited by D. R. Sherrod, W. E. Scott, and P. H. Stauffer, pages 415–424. DOI: 10.3133/pp175020.

Mueller, S., S. Lane, and U. Kueppers (2015). "Lab-scale ash production by abrasion and collision experiments of porous volcanic samples". *Journal of Volcanology and Geothermal Research* 302, pages 163–172. DOI: 10.1016/j.jvolgeores.2015.07.013.

Muthuswamy, M. and A. Tordesillas (2006). "How do interparticle contact friction, packing density and degree of polydispersity affect force propagation in particulate assemblies?" *Journal of Statistical Mechanics: Theory and Experiment* 2006(09), P09003–P09003. DOI: 10.1088/1742-5468/2006/09/p09003.

Nawaz, M. F., G. Bourrié, and F. Trolard (2013). "Soil compaction impact and modelling. A review". *Agronomy for Sustainable Development* 33(2), pages 291–309. DOI: 10.1007/s13593-011-0071-8.

Parkin, A. K. (1991). "Creep of Rockfill". *Advances in Rockfill Structures*. Springer Netherlands, pages 221–237. ISBN: 9789401132060. DOI: 10.1007/978-94-011-3206-0_9.

Poland, M. P., A. Peltier, A. Bonforte, and G. Puglisi (2017). "The spectrum of persistent volcanic flank instability: A review and proposed framework based on Kīlauea, Piton de la Fournaise, and Etna". *Journal of Volcanology and Geothermal Research* 339, pages 63–80. DOI: 10.1016/j.jvolgeores.2017.05.004.

Quane, S. L., J. K. Russell, and E. A. Friedlander (2009). "Time scales of compaction in volcanic systems". *Geology* 37(5), pages 471–474. DOI: 10.1130/g25625a.1.

Rotonda, T., P. Tommasi, and D. Boldini (2010). "Geomechanical Characterization of the Volcaniclastic Material Involved in the 2002 Landslides at Stromboli". *Journal of Geotechnical and Geoenvironmental Engineering* 136(2), pages 389–401. DOI: 10.1061/(asce)gt.1943-5606.0000218.

Saadi, F. A., K.-H. Wolf, and C. v. Kruijsdijk (2017). "Characterization of Fontainebleau Sandstone: Quartz Overgrowth and its Impact on Pore-Throat Framework". *Journal of Petroleum & Environmental Biotechnology* 08(03). DOI: 10.4172/2157-7463.1000328.

Sassa, K., K. Dang, B. He, K. Takara, K. Inoue, and O. Nagai (2014). "A new high-stress undrained ring-shear apparatus and its application to the 1792 Unzen–Mayuyama megaslide in Japan". *Landslides* 11(5), pages 827–842. DOI: 10.1007/s10346-014-0501-1.

Schaefer, L. N., F. Di Traglia, E. Chaussard, Z. Lu, T. Nolesini, and N. Casagli (2019). "Monitoring volcano slope instability with Synthetic Aperture Radar: A review and new data from Pacaya (Guatemala) and Stromboli (Italy) volcanoes". *Earth-Science Reviews* 192, pages 236–257. DOI: 10.1016/j.earscirev.2019.03.009.

Schaefer, L. N., J. E. Kendrick, T. Oommen, Y. Lavallée, and G. Chigna (2015). "Geomechanical rock properties of a basaltic volcano". *Frontiers in Earth Science* 3. DOI: 10.3389/feart.2015.00029.

Schaefer, L. N., G. Kereszturi, B. M. Kennedy, and M. Villeneuve (2023). "Characterizing lithological, weathering, and hydrothermal alteration influences on volcanic rock properties via spectroscopy and laboratory testing: a case study of Mount Ruapehu volcano, New Zealand". *Bulletin of Volcanology* 85(8). DOI: 10.1007/s00445-023-01657-w.

Schaefer, L. N., Z. Lu, and T. Oommen (2016). "Post-Eruption Deformation Processes Measured Using ALOS-1 and UAVSAR InSAR at Pacaya Volcano, Guatemala". *Remote Sensing* 8(1), page 73. DOI: 10.3390/rs8010073.

Siebert, L. (1992). "Threats from debris avalanches". *Nature* 356(6371), pages 658–659. DOI: 10.1038/356658a0.

Tang, C., X. Xu, S. Kou, P.-A. Lindqvist, and H. Liu (2001). "Numerical investigation of particle breakage as applied to mechanical crushing—Part I: Single-particle breakage". *International Journal of Rock Mechanics and Mining Sciences* 38(8), pages 1147–1162. DOI: 10.1016/s1365-1609(01)00075-2.

Torquato, S. and H. Haslach (2002). "Random Heterogeneous Materials: Microstructure and Macroscopic Properties". *Applied Mechanics Reviews* 55(4), B62–B63. DOI: 10.1115/1.1483342.

Vandewalle, N., G. Lumay, O. Gerasimov, and F. Ludewig (2007). "The influence of grain shape, friction and cohesion on granular compaction dynamics". *The European Physical Journal E* 22(3), pages 241–248. DOI: 10.1140/epje/e2007-00031-0.

Vasseur, J., F. B. Wadsworth, Y. Lavallée, K.-U. Hess, and D. B. Dingwell (2013). "Volcanic sintering: Timescales of viscous densification and strength recovery". *Geophysical Research Letters* 40(21), pages 5658–5664. DOI: 10.1002/2013gl058105.

Wadsworth, F. B., J. Vasseur, B. Scheu, J. E. Kendrick, Y. Lavallée, and D. B. Dingwell (2016). "Universal scaling of fluid permeability during volcanic welding and sediment diagenesis". *Geology* 44(3), pages 219–222. DOI: 10.1130/g37559.1.

Walding, N., R. Williams, P. Rowley, and N. Dowey (2023). "Cohesional behaviours in pyroclastic material and the implications for deposit architecture". *Bulletin of Volcanology* 85(11). DOI: 10.1007/s00445-023-01682-9.

Weaver, J., G. H. Eggertsson, J. E. P. Utley, P. A. Wallace, A. Lamur, J. E. Kendrick, H. Tuffen, S. H. Markússon, Y. Lavallée, and E. Gomez-Rivas (2020). "Thermal Liability of Hyaloclastite in the Krafla Geothermal Reservoir, Iceland: The Impact of Phyllosilicates on Permeability and Rock Strength". *Geofluids* 2020, pages 1–20. DOI: 10.1155/2020/9057193.

Wittmann, W., F. Sigmundsson, S. Dumont, and Y. Lavallée (2017). "Post-emplacement cooling and contraction of lava flows: InSAR observations and a thermal model for lava fields at Hekla volcano, Iceland". *Journal of Geophysical Research: Solid Earth* 122(2), pages 946–965. DOI: 10.1002/2016jb013444.

Won, J., B. Ryu, and H. Choo (2023). "Evolution of maximum shear modulus and compression index of rigid–soft mixtures under repetitive K0 loading conditions". *Acta Geotechnica* 19(2), pages 1047–1062. DOI: 10.1007/s11440-023-01945-x.

Wong, T.-F. and P. Baud (2012). "The brittle-ductile transition in porous rock: A review". *Journal of Structural Geology* 44, pages 25–53. DOI: 10.1016/j.jsg.2012.07.010.

Zorn, E. U., M. Vassileva, T. R. Walter, H. Darmawan, L. Röhler, and F. Amelung (2023). "Interactions of magmatic intrusions with the multiyear flank instability at Anak Krakatau volcano, Indonesia: Insights from InSAR and analogue modeling". *Geology* 51(4), pages 340–344. DOI: 10.1130/g50693.1.